

Surface transport and barrier effects in metal halide perovskites explored by bias polarity switching.

Marián Betušiak^{1*}, Roman Grill¹, Eduard Belas¹, Petr Praus¹, Mykola Brynza¹, Mahshid Ahmadi^{2*}, Jonghee Yang³, Artem Musiienko⁴,

¹ , *Institute of Physics, Faculty of Mathematics and Physics, Charles University, Ke Karlovu 5, CZ 121 16 Prague, Czech Republic*

*majo.betusiak@gmail.com

² *Joint Institute for Advanced Materials, Department of Materials Science and Engineering, University of Tennessee, Knoxville, TN 37996, USA.*

*mahmadi3@utk.edu

³ *Department of Chemistry, Yonsei University, Seoul 03722, Republic of Korea*

⁴ *Helmholtz Zentrum Berlin für Materialien und Energie GmbH, Berlin, Germany*

Abstract

Popular summary

Highlights

1. The charge transport in metal halide perovskites was studied in the dark and by photoconductivity and transient current techniques with specific concern to the defect structure in contact-perovskite interface.
2. It was testified that a significant barrier at the interface delays the drain of holes to the cathode.
3. Holes accumulated at the interface remain partly free being able to immediately leave the contact after polarity switch.
4. Remaining accumulated charge is deliberated from the interface by a mechanism that is independent of bias.

I Introduction

Metal halide perovskites (MHP) sparked an interest of scientific community in 2009 when they were first incorporated into a solar cell [1]. Since then, MHP were investigated for use in resistive [2] and photon-counting [3] detectors, light emitting diodes, quantum dot color filters [4], [5] or scintillators [6].

Unlike CdTe or GaAs, where the performance of optoelectronic devices is limited by crystal defects, in perovskites the main issue is their inherent instability. These materials exhibit considerable ionic drift which can lead to electric field distortion, chemical reaction of halides with contact, interfacial layer or surrounding environment [7]. Consequently, a number of works identify interfaces as a primary source of perovskite instability and emphasize the importance of surface passivation and preparation of the transport layers [7], [8], [9], [10], [11], [12]. Properly engineered transport layers can also

mitigate the accumulation of electronic charge carriers at collecting electrodes, a phenomenon reported to induce phase segregation in mixed-halide perovskites [8], [9], [10].

In halide perovskite single crystals, surface processes are localized in a thin region typically $\leq 1 \mu\text{m}$ below interface. Their investigation is therefore experimentally challenging. Kelvin probe microscopy [14], conductive atomic force microscopy [15] and photoluminescence microscopy [16] were used to study the surface phenomena before, however, they offer very limited depth information which makes them not suitable for planar-planar devices.

These effects were previously analyzed by impedance spectroscopy [7], [13], , photoluminescence microscopy [16].

Here we explore the surface properties in metal halide perovskites using the photocurrent relaxations and fast bias switching. The main idea is to take advantage of the accumulated charge carriers and study their dynamics after the bias polarity switch at various biases, and temperatures.

II Experimental

Photocurrents after bias polarity switch (BiPS)

The experiment is based on the measurement of the current response of the sample to the above-bandgap (520 nm/2.38 eV) optical pulse (100 μs). The current is measured as the voltage drop on 1 k Ω readout resistor and recorded by an oscilloscope. The detailed scheme of the setup is presented in Fig.1 a). In order to suppress the effects of ionic drift we use rectangular bipolar bias pulses that satisfy $U^+T_b^+ = U^-T_b^-$, where U^+ , U^- represent the applied bias and T_b^+ , T_b^- are the bias pulse widths in respective polarities. The bias pulse is then followed by depolarization time DT that allows sample relaxation (typically >100ms). The timing of the bias and optical pulse is shown in Fig. 1 b). In order to further suppress signal drift over the course of the measurement, each sequence of pulsing parameters (200 bias cycles) was repeated 4-8 times during one measurement and averaged. This procedure reveals signal drift (if present), or spreads the drift more evenly to all measured points in the sequence. The dark current was measured more often (every 20 bias cycles)

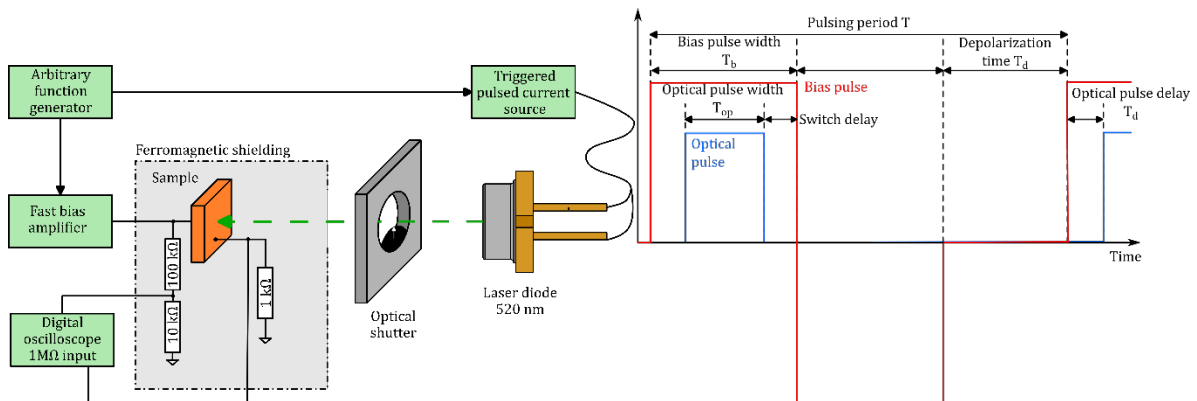


Fig. 1: a) Schematic diagram of the setup for photocurrent measurement. b) Bias and optical pulse timing diagram.

III Results and discussion

In Fig. 2 we present the photocurrent relaxations in CsPbBr₃ sample. In the experiment, the parameters of the first negative pulse $U^- = 150$ V and $T_b^- = 1$ ms were kept constant and only the amplitude U^+ and width T_b^+ of the second pulse was changed ($U^+T_b^+ = U^-T_b^-$). In the first bias pulse we observed standard behaviour – no photocurrent before illumination, sharp increase and relaxation during illumination and draining of photocarriers after the light is switched off. However, after the polarity switch there is a temporary increase of photocurrent again. It cannot be attributed to the RC relaxation of the sample since it is subtracted with the dark current (see Fig. S1). Also, as can be seen in detail in Fig. 2 b) this effect is bias-dependent, unlike RC relaxation.

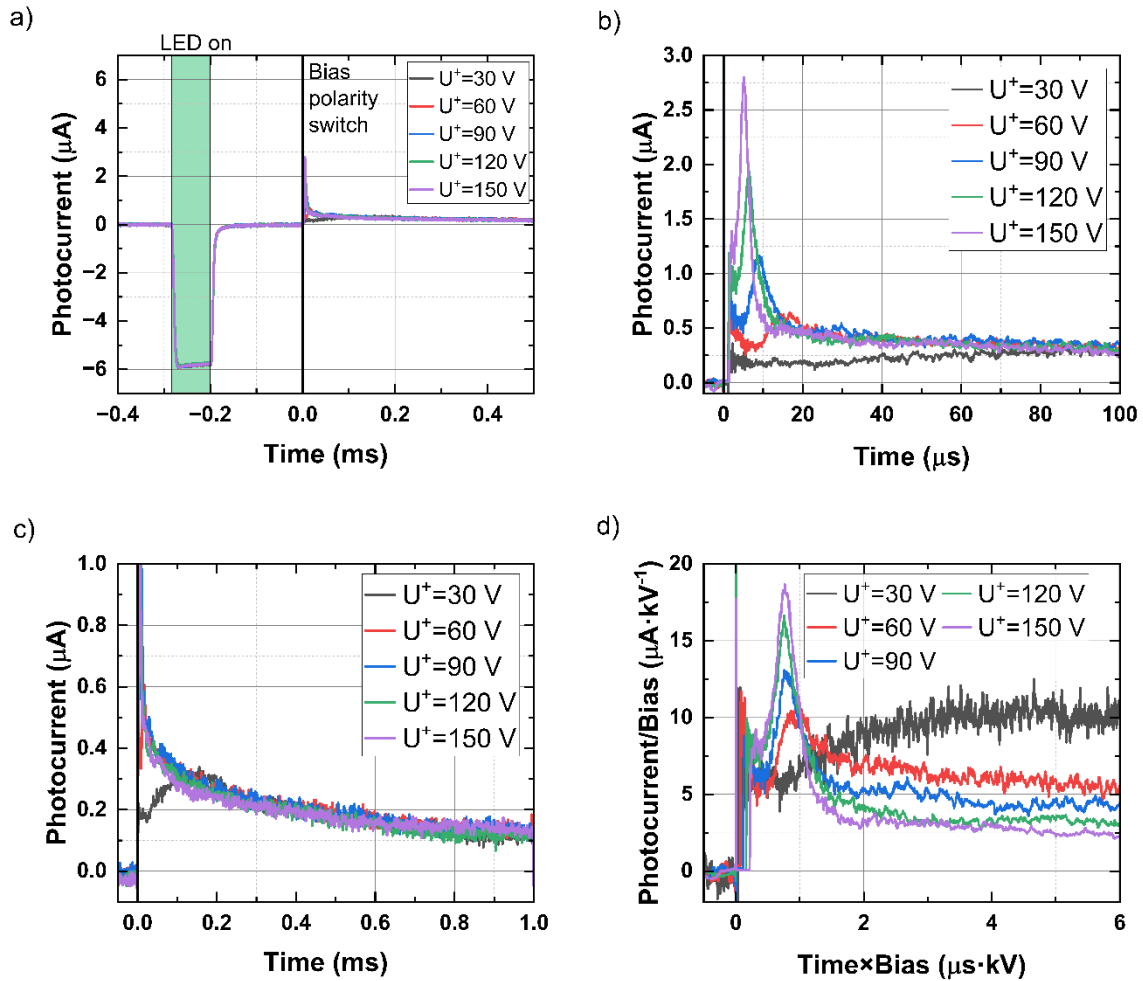


Fig.2: a) Photocurrent relaxation before and after bias polarity switch. b) Detail of the photocurrent relaxation after bias polarity switch. c) Detail of the tails of the BiPS waveforms. d) Bias normalized BiPS waveforms. Only the positive bias pulse amplitude U^+ and width T_b^+ is changed in the experiment, $U^- = 150$ V and $T_b^- = 1$ ms and $DT = 200$ ms are kept constant.

We then compared the photocurrent relaxation in Fig. 2 b) with the hole waveforms (CWF) measured in the same sample by laser-induced transient current technique (L-TCT) [17], [18] under the same biasing conditions. Measured current waveforms are shown in Fig.3 a). We see that carriers drifting in both experiments show nearly the same transit time, which testifies to the identical species responsible for both phenomena. Transit time t_{tr} , represents the time it takes charge carriers to pass whole sample. It is determined as a time between of the half-maximum of the rising and falling edges

in L-TCT, and the delay between the polarity switch ($t=0$ s) and half-maximum of the falling edge (after the peak in Fig. 2 b) in the BiPS experiment. In addition, unlike from L-TCT-CWFs, BiPS-CWFs reveals also a significant bias-independent tail Fig. 2 c) caused by the emission of charge carriers temporarily captured near the perovskite-contact interface. However, the experiment cannot identify the specific type of charge carriers responsible tail. If the data in Fig. 2 b) are treated as classical current waveforms assuming constant internal electric field, carrier mobility $\mu_{TCT}=20 \text{ cm}^2\cdot\text{V}^{-1}\cdot\text{s}^{-1}$ and $\mu_{ph}=23 \text{ cm}^2\cdot\text{V}^{-1}\cdot\text{s}^{-1}$ can be evaluated using the formula

$$\mu = \frac{L^2}{t_{tr}U} [19].$$

Difference of the evaluated mobility and the non-constant shape of the current responses can be linked to the warped electric field due to ionic drift [20], charge de-/trapping [21], or plasma effect [22] where moving charge screens the applied electric field and affects its own drift. Considering the relative permittivity $\epsilon_{CsPbBr_3} = 16.5$ [23], the charge density (of uniformly charged plane) required to completely screen applied electric field ($1.1 \text{ kV}\cdot\text{cm}^{-1}$) is roughly $3.2 \text{ nC}\cdot\text{cm}^{-2}$. Given the photogenerated charge density in the experiment is roughly $3.1 \text{ nC}\cdot\text{cm}^{-2}$, the plasma effect plays important role. Waveforms modeled for different charge concentrations are presented in Fig. S2. The shape of the modeled waveforms is given by the acceleration (coulombic repulsion) of the front of the charge packet forming peak before the expected transit time. On the other hand, the back of the charge packet is slowed down and forms tail. Disregarding the tail, there is a resemblance between the polarity switch CWFs in Fig.2 b) and the modeled CWF with plasma effect in Fig. S2. The presence of the plasma effect is further corroborated by the elongation of the transit time at 30 V and 60 V, where the plasma effect is stronger. This is highlighted in bias-normalized CWFs in Fig. 2 d) as a transit time shift at low biases. The bias normalization is used to remove expected CWF amplitude and width bias dependence while still conserving overall shape and charge. On the other hand, the transit time of the bias-normalized TCT-CWFs in Fig. 3 b) is shorter at low biases. This corresponds to super-linearly increasing space charge. In the case of BiPS the space charge causing the electric field deformation is either constant (plasma effect) or increases sub-linearly.

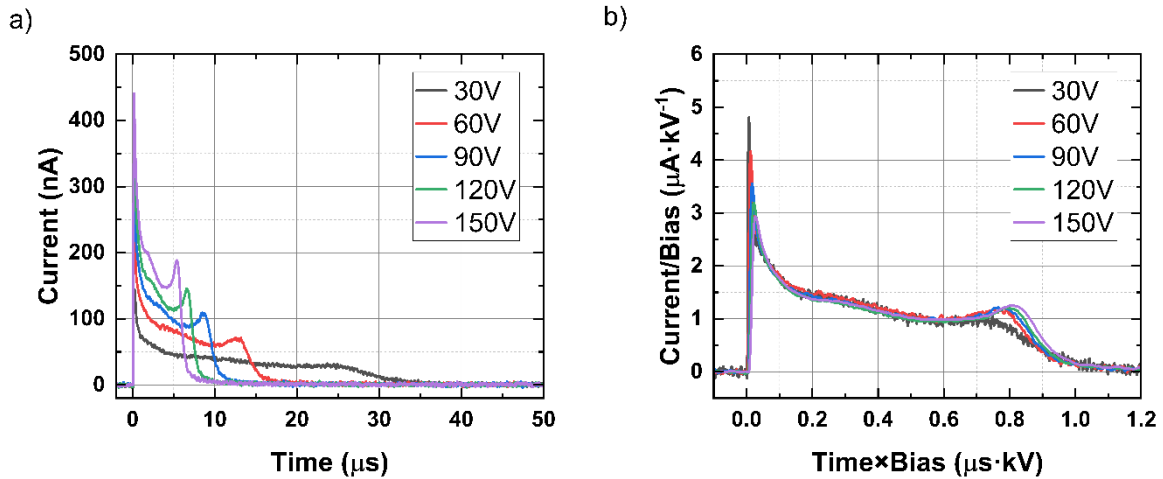


Fig.3: a) Bias dependent of the hole transient current waveforms measured by L-TCT. b) Bias-normalized L-TCT waveforms.

All of these results lead to a simple model of accumulation of free and trapped holes beneath the cathode barrier depicted in Fig. 4. After the bias polarity is switched, the accumulated still-free holes immediately drift to the new cathode (anode in previous polarity) and induce a typical TCT signal as was demonstrated in Fig 2 b) while holes released from traps produce the long tail. According to modelled current waveforms in Fig. S2 the plasma effect can also contribute to the tail but only in timescale comparable with transit time.

In model shown in Fig. 4, accumulated holes can i) tunnel through or thermally jump over the barrier, ii) hop through defects in amorphous/polycrystalline barrier or damaged surface layer, iii) be trapped or iv) recombine with injected electrons at surface defects.

Considering the distribution of holes near the interface (barrier at $x=0$) ruled by the Boltzmann statistics, the distribution of accumulated carriers is expressed $p(x) = p_0 e^{-\frac{eU}{k_B T L} x}$ where p_0 is the charge concentration at the barrier, L is the width of the sample, e is elementary charge, k_B is Boltzmann constant and T is the temperature. For example, in the measured sample at 150 V, holes should accumulate in a region ~ 230 nm wide. Therefore, this experiment has a potential to probe surface/barrier properties and determine the mode of accumulated hole dissipation.

Because of the use of the optical pulse for excitation, we know the amount of generated holes. Therefore, the accumulation efficiency of free holes η_{tr} and overall accumulation efficiency η can be determined. The η_{tr} is defined as the ratio of the charge collected from the polarity-switch-signal until the transit time (half of the falling edge of the peak) to the whole photogenerated charge. The overall accumulation efficiency η also includes holes detrapped from defects.

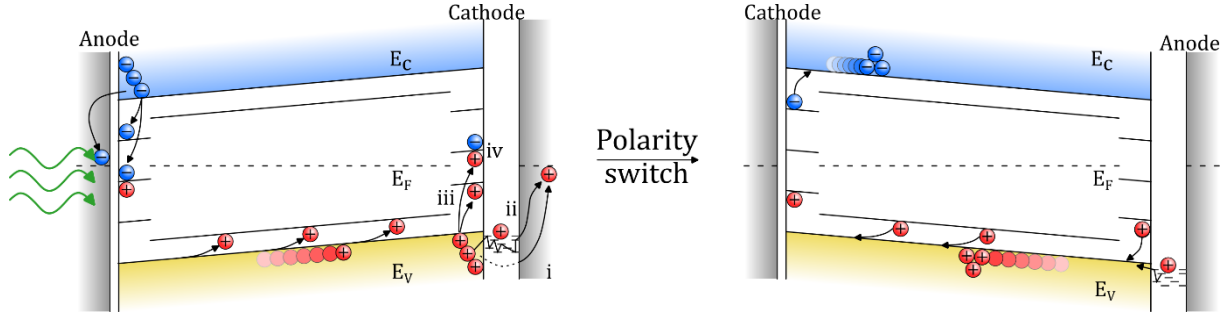


Fig. 4: Model of the accumulation of the holes beneath the cathode barrier. Free holes dissipate/disappear by i) tunneling through or thermal excitation over barrier, ii) hopping through barrier or surface layer defects, iii) trapping or iv) recombination in the surface defects.

To characterize the effect of the bias pulse width and amplitude we measured the accumulation efficiency of holes shown in Fig. 5 depending on laser pulse delay, while the switch delay (SD) was kept constant $SD=200 \mu s$ (Fig.1 b). In this experiment, the bias pulses were symmetrical $U^+=U^-$, $T^+=T^- = OPD+300 \mu s$.

The accumulation efficiency of free holes in Fig. 5 drops by roughly the same amount as the overall efficiency η . This means that the number of trapped holes is the same regardless the length of the bias application (up to 10 ms). Because the switch delay and photogenerated charge are the same in this experiment, the η_{tr} can change only due to variable surface layer properties. Decrease of the signal suggests either increased trapping Fig. 4 iii) or recombination Fig. 4 iv) or by accelerated draining of the accumulated carriers Fig. 4 i), Fig. 4 ii). However increased recombination/trapping would affect also trapped holes forming tail, unless the trapping time is significantly shorter and

detrapping significantly longer than fixed delay 200 μs (trapped holes are not in equilibrium with free holes). It is also possible that the tail is caused by other charge carriers for example detrapping of electrons accumulated beneath anode. Lastly considering the spatial inhomogeneities of the surface layer, free holes can accumulate in a different region than trapped holes. However, these regions need to be distinctly separated to explain different behaviour of free and trapped carriers.

The tunneling of holes into the contact is improbable due to the strong temperature dependence of the accumulated hole density (Fig. S4), which excludes the tunneling phenomena from the consideration.

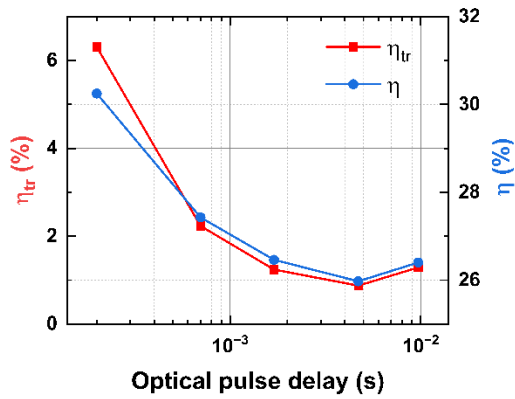


Fig.5 Dependence of the fraction of the accumulated free holes and all accumulated holes on optical pulse delay at various biases. Experiment was done at $U^+=U^-=150$ V, $T_b^+=T_b^-=200$ μs -20 ms, $DT=200$ ms.

Next, we studied the extinction of the accumulated free holes by the prolongation of the bias polarity switch delay SD (see Fig.1 b) at $U^+=U^-=150$ V. In this experiment the bias pulse width was kept the same $T^+=T^-=21$ ms, only the delay of the optical pulse and SD was changed. As expected, the number of accumulated free holes, shown in Fig. 6, decay with increasing switch delay. Given the longer bias pulses, the effect of equilibrium holes can be observed only for switch delay 10 ms or longer ($OPD < 10$ ms).

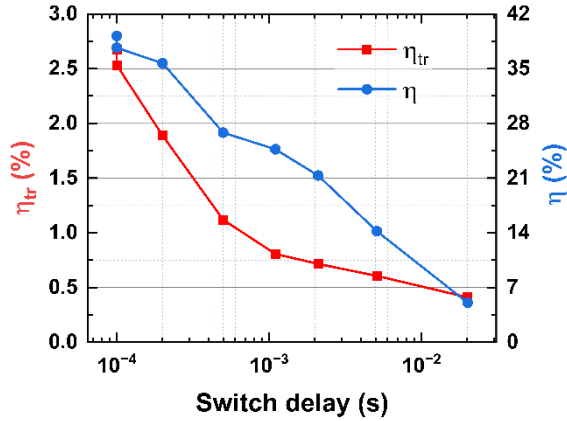


Fig. 6: Dependence of the accumulated free holes and all accumulated holes on the switch delay. Experiment was done at $U^+ = U^- = 150$ V, $T_b^+ = T_b^- = 21$ ms, $DT = 200$ ms.

Next we measured the temperature dependence to further probe proposed model. Measured dependencies are shown in Fig. 7 a). Only for the models with classical barrier or hopping through barrier defects, the free hole accumulation efficiency is expected to increase after cooling the sample down. In the defective-surface-layer model, at low temperatures the detrapping from the shallow defects slows down, essentially turning them into deep traps, which lowers the number of free holes.

In the model of classical barrier, the tails of the polarity-switch waveforms are caused by detrapping from the surface states. While in the hopping model, tails are formed by the hopping out of the barrier defects. Both are thermally activated but the hopping tail also depends on the position of the carriers in the barrier layer. At low temperatures, carriers hop only into thin layer compared to the high temperatures, which should decrease collected charge from the tail and also shorten the tail relaxation time as can be seen in Fig. S4.

The decay of the signal in Fig. 7 a) is dependent also on the dark current which is expected to decrease at low temperatures. The accumulation efficiency of the free holes is the combination of the opposing effects. First, decreasing dark current that empties defects in barrier allowing faster hopping of photogenerated holes. Second, slowing down of hopping which leaves more accumulated carriers outside of the barrier. This accumulation is so strong below 210 K it leads to memory effects – photogenerated carriers accumulate during consecutive bias/optical pulses. Because of this we only show data only up to 210 K, where the dark current was stable throughout the measurements. In Fig. 7 b) we evaluated the activation energies $E_1 = 150$ meV and $E_2 = 770$ meV of the hole dissipation. Given the relatively small temperature range evaluated values are only rough estimates. The higher activation energy E_2 correspond to the barrier height, while E_1 is likely an activation energy of the hopping through the barrier defects.

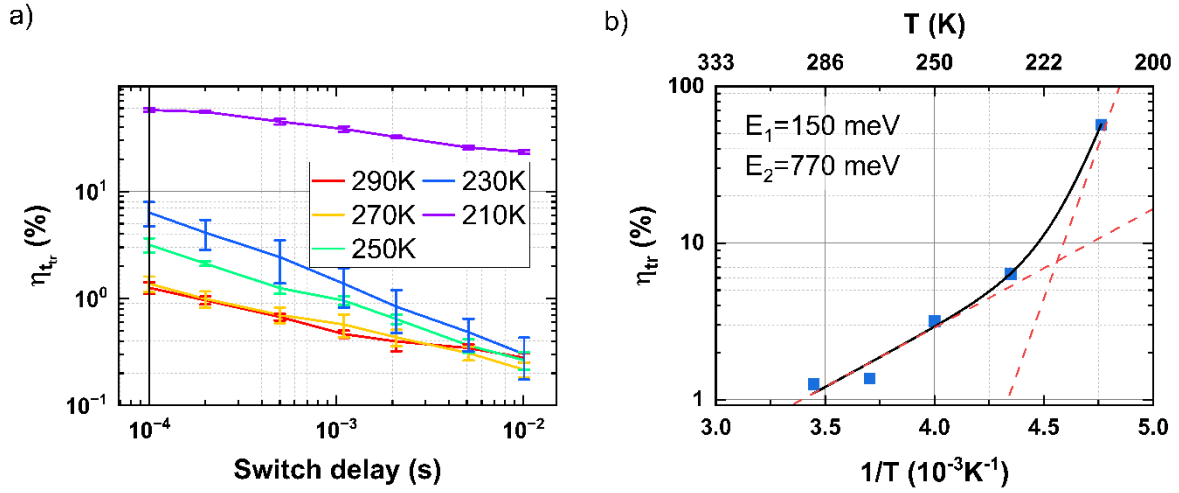


Fig.7: a) Dependence of the accumulated free holes at different temperatures. b) Temperature dependence of accumulation efficiency of free holes at switch delay 100 μ s. Experiment was done at $U^+ = U^- = 150$ V, $T_b^+ = T_b^- = 11$ ms, $DT = 200$ ms.

Lastly, we repeated the same experiments in MAPbBr₃ sample with Cr/MAPbBr₃/SnO₂/Cr contacts. The switch delay dependences in Fig. 8 a) show even stronger accumulation than in CsPbBr₃ sample. Surprisingly, accumulation efficiency of free holes is higher underneath the Cr contact even despite the fact that SnO₂ as an electron transport layer [24] should block holes. That means that either Cr reacts with perovskite and produces interfacial barrier layer, or SnO₂ better protects the sample from atmospheric degradation.

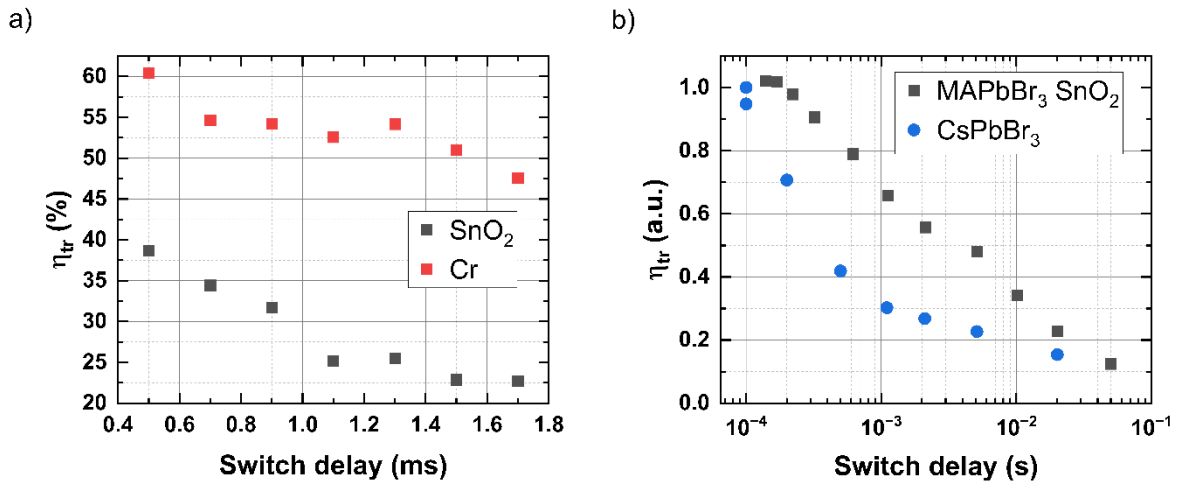


Fig. 8: a) Dependence of accumulation efficiency in MAPbBr₃ on switch delay. Holes accumulate under /SnO₂/Cr or /Cr contact. b) Comparison of normalized switch delay dependence of accumulated free holes in CsPbBr₃ and MAPbBr₃ sample.

IV Conclusion

The bias polarity switching proved accumulation of photo-generated holes beneath cathode in CsPbBr₃ and MAPbBr₃ samples. Further experiments done at various optical pulse delays and bias

polarity switch delays suggest that hole exit the sample mainly in specific spots allowing direct penetration through the barrier then by hopping transport through the barrier localized states .

Acknowledgments

This research was supported by the Grant Agency of Charles University under contract No GAUK 393222 and by the Grant Agency of the Czech Republic under contract number 23-07951S.

Supplementary

Sample preparation

CsPbBr₃ sample was grown by vertical Bridgman technique at Charles University. Wafers were polished by Al₂O₃ in oil, rinsed in toluene, etched in DMSO for 1 minute and rinsed again in toluene. Planar contacts with guard ring structure were prepared by thermal evaporation of chromium (~50nm) and connected to the sample holder via silver wires and conductive paint. In order to reach good thermal contact, the sample was secured flat to the holder by a thermal paste.

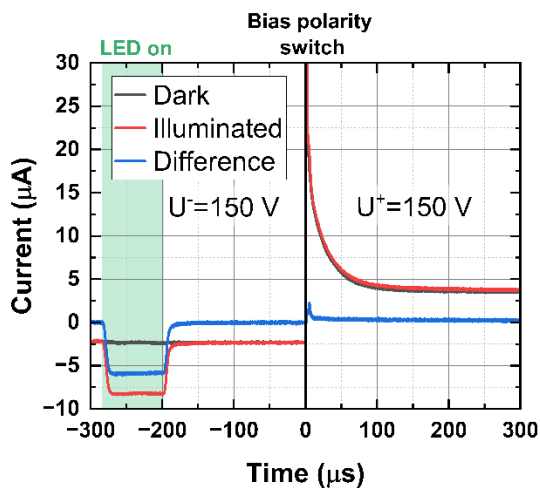


Figure S1: Current relaxation in dark and under illumination. Bias pulse parameters $U^+ = U^- = 150$ V, $T_b^+ = T_b^- = 1$ ms, $DT = 200$ ms.

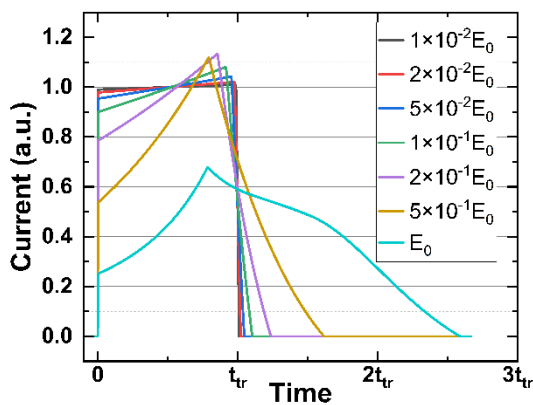


Figure S2: Simulated current waveforms for different photogenerated charge densities expressed in terms of applied electric field E_0 . 1D geometry is assumed in the simulation.

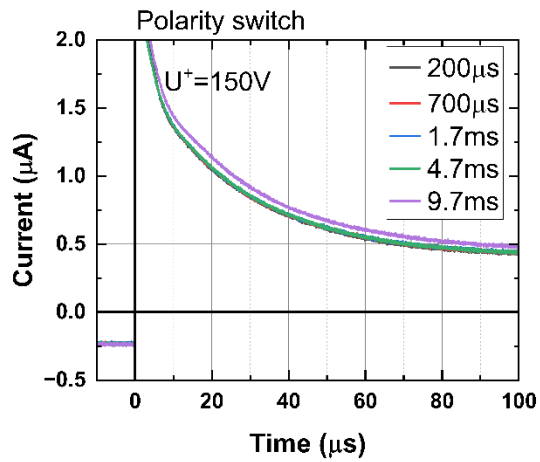


Figure S3. Dependence of the dark current measured concurrently with data in Fig. 5 a) on the laser pulse delay.

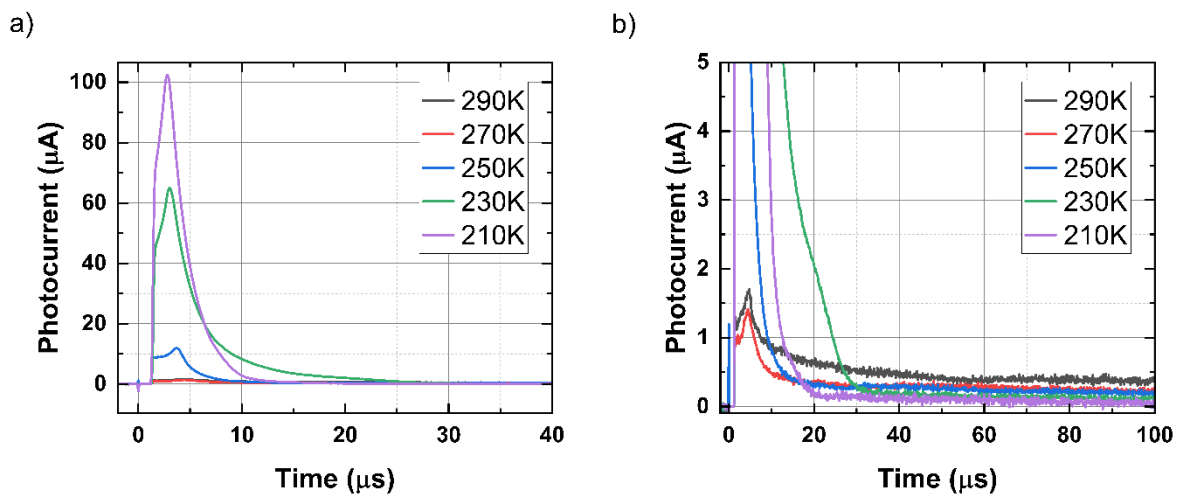


Fig. S4: a) Temperature dependence of BiPS waveforms b) Detail of BiPS waveform tails. Experiment was done at $U^+ = U^- = 150$ V, $T_b^+ = T_b^- = 11$ ms, $DT = 200$ ms and switch delay 300 μ s.

References

- [1] A. Kojima, K. Teshima, Y. Shirai, and T. Miyasaka, "Organometal Halide Perovskites as Visible-Light Sensitizers for Photovoltaic Cells," *J. Am. Chem. Soc.*, vol. 131, no. 17, pp. 6050–6051, May 2009, doi: 10.1021/ja809598r.
- [2] A. Ciavatti *et al.*, "High-Sensitivity Flexible X-Ray Detectors based on Printed Perovskite Inks," *Adv. Funct. Mater.*, vol. 31, no. 11, p. 2009072, 2021, doi: 10.1002/adfm.202009072.

- [3] Y. He *et al.*, “CsPbBr₃ perovskite detectors with 1.4% energy resolution for high-energy γ -rays,” *Nat. Photonics*, vol. 15, no. 1, Art. no. 1, Jan. 2021, doi: 10.1038/s41566-020-00727-1.
- [4] “State of the Art and Prospects for Halide Perovskite Nanocrystals | ACS Nano.” Accessed: Aug. 31, 2024. [Online]. Available: <https://pubs.acs.org/doi/full/10.1021/acsnano.0c08903>
- [5] Y.-H. Ko, M. Jalalah, S.-J. Lee, and J.-G. Park, “Super Ultra-High Resolution Liquid-Crystal-Display Using Perovskite Quantum-Dot Functional Color-Filters,” *Sci. Rep.*, vol. 8, no. 1, p. 12881, Aug. 2018, doi: 10.1038/s41598-018-30742-w.
- [6] M. D. Birowosuto *et al.*, “X-ray Scintillation in Lead Halide Perovskite Crystals,” *Sci. Rep.*, vol. 6, no. 1, p. 37254, Nov. 2016, doi: 10.1038/srep37254.
- [7] M. Ahmadi *et al.*, “Environmental Gating and Galvanic Effects in Single Crystals of Organic–Inorganic Halide Perovskites,” *ACS Appl. Mater. Interfaces*, vol. 11, no. 16, pp. 14722–14733, Apr. 2019, doi: 10.1021/acsaami.8b21112.
- [8] X. Tang *et al.*, “Local Observation of Phase Segregation in Mixed-Halide Perovskite,” *Nano Lett.*, vol. 18, no. 3, pp. 2172–2178, Mar. 2018, doi: 10.1021/acs.nanolett.8b00505.
- [9] L. A. Frolova *et al.*, “Reversible Pb²⁺/Pb⁰ and I⁻/I₃⁻ Redox Chemistry Drives the Light-Induced Phase Segregation in All-Inorganic Mixed Halide Perovskites,” *Adv. Energy Mater.*, vol. 11, no. 12, p. 2002934, 2021, doi: 10.1002/aenm.202002934.
- [10] J. T. DuBose and P. V. Kamat, “Hole Trapping in Halide Perovskites Induces Phase Segregation,” *Acc. Mater. Res.*, vol. 3, no. 7, pp. 761–771, Jul. 2022, doi: 10.1021/accountsmr.2c00076.
- [11] Z. Zhu *et al.*, “Spatial Control of the Hole Accumulation Zone for Hole-Dominated Perovskite Light-Emitting Diodes by Inserting a CsAc Layer,” *ACS Appl. Mater. Interfaces*, vol. 15, no. 5, pp. 7044–7052, Feb. 2023, doi: 10.1021/acsaami.2c19230.
- [12] B. Wu *et al.*, “Charge Accumulation and Hysteresis in Perovskite-Based Solar Cells: An Electro-Optical Analysis,” *Adv. Energy Mater.*, vol. 5, no. 19, p. 1500829, 2015, doi: 10.1002/aenm.201500829.
- [13] A. Guerrero, J. Bisquert, and G. Garcia-Belmonte, “Impedance Spectroscopy of Metal Halide Perovskite Solar Cells from the Perspective of Equivalent Circuits,” *Chem. Rev.*, vol. 121, no. 23, pp. 14430–14484, Dec. 2021, doi: 10.1021/acs.chemrev.1c00214.
- [14] M. Ahmadi, L. Collins, K. Higgins, D. Kim, E. Lukosi, and S. V. Kalinin, “Spatially Resolved Carrier Dynamics at MAPbBr₃ Single Crystal–Electrode Interface,” *ACS Appl. Mater. Interfaces*, vol. 11, no. 44, pp. 41551–41560, Nov. 2019, doi: 10.1021/acsaami.9b16287.
- [15] Y. Shao *et al.*, “Grain boundary dominated ion migration in polycrystalline organic–inorganic halide perovskite films,” *Energy Environ. Sci.*, vol. 9, no. 5, pp. 1752–1759, May 2016, doi: 10.1039/C6EE00413J.
- [16] C. Li, A. Guerrero, S. Huettner, and J. Bisquert, “Unravelling the role of vacancies in lead halide perovskite through electrical switching of photoluminescence,” *Nat. Commun.*, vol. 9, no. 1, p. 5113, Nov. 2018, doi: 10.1038/s41467-018-07571-6.
- [17] J. Pipek *et al.*, “Charge Transport and Space-Charge Formation in $\text{Cd}_{1-x}\text{Zn}_x\text{Te}_{1-y}\text{Se}_y$ Radiation Detectors,” *Phys. Rev. Appl.*, vol. 15, no. 5, p. 054058, May 2021, doi: 10.1103/PhysRevApplied.15.054058.
- [18] A. Musiienko *et al.*, “Deciphering the effect of traps on electronic charge transport properties of methylammonium lead tribromide perovskite,” *Sci. Adv.*, vol. 6, no. 37, p. eabb6393, Sep. 2020, doi: 10.1126/sciadv.abb6393.
- [19] A. Musiienko *et al.*, “Characterization of polarizing semiconductor radiation detectors by laser-induced transient currents,” *Appl. Phys. Lett.*, vol. 111, no. 8, p. 082103, Aug. 2017, doi: 10.1063/1.4997404.
- [20] A. O. Alvarez *et al.*, “Ion Migration and Space-Charge Zones in Metal Halide Perovskites Through Short-Circuit Transient Current and Numerical Simulations,” *Adv. Electron. Mater.*, vol. 10, no. 11, p. 2400241, 2024, doi: 10.1002/aelm.202400241.

- [21] J. Franc, V. Dědič, P. J. Sellin, R. Grill, and P. Veeramani, "Radiation induced control of electric field in Au/CdTe/In structures," *Appl. Phys. Lett.*, vol. 98, no. 23, p. 232115, Jun. 2011, doi: 10.1063/1.3598414.
- [22] K. Suzuki, Y. Ichinohe, and S. Seto, "Effect of Intense Optical Excitation on Internal Electric Field Evolution in CdTe Gamma-Ray Detectors," *J. Electron. Mater.*, vol. 47, no. 8, pp. 4332–4337, Aug. 2018, doi: 10.1007/s11664-018-6245-2.
- [23] J. Song *et al.*, "Ultralarge All-Inorganic Perovskite Bulk Single Crystal for High-Performance Visible–Infrared Dual-Modal Photodetectors," *Adv. Opt. Mater.*, vol. 5, no. 12, p. 1700157, 2017, doi: 10.1002/adom.201700157.
- [24] X. Ren *et al.*, "Solution-Processed Nb:SnO₂ Electron Transport Layer for Efficient Planar Perovskite Solar Cells," *ACS Appl. Mater. Interfaces*, vol. 9, no. 3, pp. 2421–2429, Jan. 2017, doi: 10.1021/acsami.6b13362.